Microchemical Journal 137 (2018) 473–479

Contents lists available at ScienceDirect

Microchemical Journal

journal homepage: www.elsevier.com/locate/microc

Energy-resolved neutron tomography of an unconventional cultured pearl at a pulsed spallation source using a microchannel plate camera

G. Vitucci [a,*], T. Minniti [b], D. Di Martino [a], M. Musa [c], L. Gori [c], D. Micieli [d], W. Kockelmann [b], K. Watanabe [e], A.S. Tremsin [f], G. Gorini [a]

[a] University of Milano Bicocca, Dept. Phys., 20126 Milan, Italy
[b] STFC-Rutherford Appleton Laboratory, ISIS Facility, Harwell OX11 0QX, UK
[c] GECI – Gemological Education Certification Institute, Milan, Italy
[d] Dip. di Fisica, Università della Calabria, via Pietro Bucci, 87036 Arcavacata di Rende, (Cosenza), Italy
[e] Nuclear Measurement Engineering Group, Nagoya University, Nagoya, 464-8603, Japan
[f] University of California at Berkeley, Space Science Laboratory, CA 94720 Berkeley, USA

ARTICLE INFO

Article history:
Received 31 August 2017
Received in revised form 29 November 2017
Accepted 5 December 2017
Available online 6 December 2017

Keywords:
Microchannel plate
Neutron imaging detector
Energy resolved imaging
Neutron phase mapping
Cultured pearl

ABSTRACT

A non-destructive neutron analysis technique performed at the IMAT beamline of the STFC (Science and Technology Facility Council), UK, is presented. In this experiment, neutrons of different energy have been exploited to obtain a tomographic reconstruction of a biomineralic sample, more specifically a cultured pearl, by using a time-resolving pixel camera, the MicroChannel Plate (MCP) detector, utilizing an array of 2 × 2 Timepix readout chips. The MCP camera is capable of energy-resolved two-dimensional mapping of neutron transmission with a spatial resolution of ~55 μm. By using a Simultaneous Iterative Reconstruction Technique (SIRT), virtual sections of the internal part of the sample have been created, thus revealing several features inside its bulk. The crystallographic phase map via Bragg edge analysis, showing a phase fraction distribution on the entire specimen, has been generated as well. Finally, 3D volume rendering of the pearl is presented.

1. Introduction

Neutron-based tomography is a non-destructive analysis technique with several advantages, such as the ability to distinguish isotopes of the same element, the high sensitivity to hydrogen and the penetration capability towards bulky materials.

The experiment described in this paper has been performed at the Imaging and Materials Science & Engineering (IMAT) beamline operating at the ISIS spallation neutron source (UK). This instrument is able to operate energy-selective neutron imaging, exploiting the time-of-flight (TOF) analysis technique enabled by the accelerator-based pulsed neutron source located in the research center [1]. The device used for the energy-dispersive neutron imaging setup was a MicroChannel Plate (MCP) neutron counting detector.

The MCP detector developed at the University of California at Berkeley in collaboration with Nova Scientific [2] is a novel neutron camera capable to perform energy-dispersive neutron radiographies and tomographies. The neutron conversion into electrons in the detector is performed by an MCP doped with ^{10}B atoms (8 μm pores on 11 μm centers). The charged particles produced in the MCP induce an electronic avalanche resulting in 10^4–10^5 electrons which are collected by the Timepix array, a pixel readout chip developed at CERN [3]. The crucial feature of this chip is the possibility to operate in "event timing" mode, enabling time-tagging each detected neutron and thus determining its energy by the time of flight technique at a pulsed neutron source. At present, the detector has a 28 × 28 mm^2 active area, with 55 μm pixel size [4].

Several experiments have been carried out in the past years on inorganic samples [5–6], demonstrating the advantages of the TOF transmission imaging technique. In this paper we show how the field of cultural heritage can take a huge advantage from this kind of non-destructive (ND) analysis, because of the rarity and non-repeatability of the specimens studied, as well as their complex bulk microstructure.

This paper focuses on the analysis of an organic sample, more specifically on a cultured pearl, by means of time-resolved neutron tomography.

* Corresponding author at: Dipartimento di Fisica "G. Occhialini", Piazza della Scienza 3, - 20126 Milano, – Italy.
E-mail address: g.vitucci@campus.unimib.it (G. Vitucci).

https://doi.org/10.1016/j.microc.2017.12.002
0026-265X/

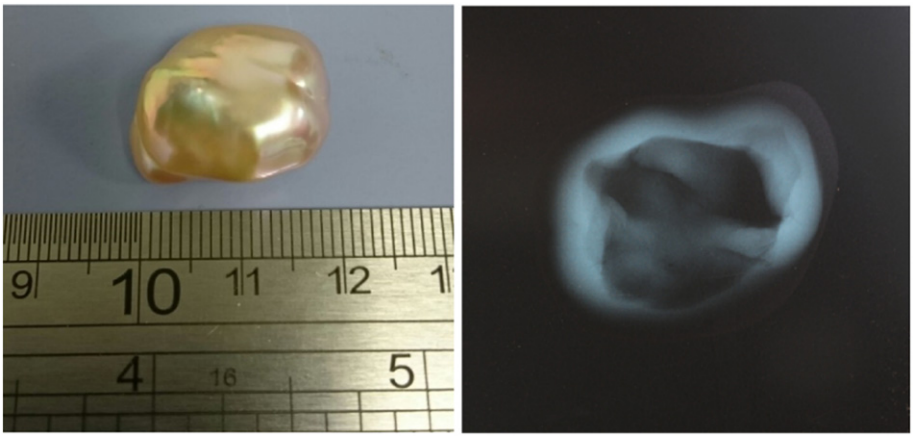

Fig. 1. Left: image of the study-case pearl. Right: X-ray radiography of the pearl.

2. Material and methods

2.1. Pearl description

During their evolution, molluscs have developed an external calcified structure, the *shell*, to support and protect their soft bodies. In the natural environment pearls are generated by accidental events, involving the activation of the same biogenic mechanisms responsible for the shell creation, but inside the living molluscs tissues. For this reason, natural pearls are rare objects, characterized by very complex biogenic structures in which the inorganic component, calcium carbonate, accounts for about 95%–99% of weight and the remaining 1% to 5% represent an organic matrix [7].

The beauty of pearls is correlated to surface features, for example the color, the luster, or the overtone; all these properties are due to the biomineralic structure of pearls. In natural pearl the calcium carbonate, constituting the inorganic component, presents two different polymorphs: a calcite phase with prismatic habitus in the inner part of the pearl, while the external area, called *nacre*, is made by an aragonite phase crystallized in flat tablets arranged in a "brick-wall" structures [8], able to interact with the light and determine the iridescent aspect of the pearl surface. It must be highlighted that all the mineral characteristics of inorganic component, like the phase, the shape, the dimension and the orientation of crystals, are self-assembled and strongly controlled by the proteins constituting the biological matrix. The nacreous aragonite tablets in fact are all iso-orientated and isometric crystals, with parallel c-axis [9].

Pearls are very important for the jewelry industry and, whereas the natural ones are rare, since the beginnings of 1900s the pearls availability started to grow by means of a culturing process which allowed the marketing of large quantities of pearls at a lower cost.

Today the culturing techniques are very sophisticated, therefore it has become difficult to distinguish between cultured and natural pearls, even though it is an essential requirement for the market [10]. In this frame, we proposed the study and characterization of pearls of different size and shapes with a novel approach, that is a non-destructive neutron analysis technique. Among the set of samples studied, in this paper we present the results obtained with an atypical-bead cultured pearl (Fig. 1). The main gemological properties of the pearl are reported in Table 1. This particular type of pearl, commercially named "soufflé", represents one of the strange types of culturing experiments, consequently of the innovative material used as nucleus. In recent years in fact, there have been many attempts to use alternative pearls and shell materials as nuclei. This includes different types of shells, bironite, laminated/powdered shell, freshwater cultured pearls and even natural pearls [11–13].

The peculiar method used to produce soufflé pearls, was intended as an intermediary step to growing large round bead cultured pearls, but the outcome resulted in very large baroque cultured pearls. The innovation consists in the use of a hydrophilic and expansible material as nucleus, from cheaper dried mud ball to more complex organic nuclei which have similar properties to super absorbent polymer spheres [13].

In this process, after a smaller cultured pearl is harvested, the hydrophilic bead is inserted into the now vacant pearl sac. Placed back in the water the bead begins to grow. As the nucleus absorbs water it expands the pearl sac in the process, determining the size and the shape of pearl [12].

At the end of pearl generation process the nucleus could be degraded or not. In the first case the pearl drilling allows the water and organic residue to come out. In the case of more complex bead, the observation of some residue inside the pearl could be possible by means of X-ray imaging, also after drilling [12]. Normally a part of the decomposed bead sediments in layers on the first nacre structure. The pearl for this study-case is not drilled.

In order to have a basis for comparison, we first acquired an X-ray 2D image of the pearl (Fig. 1, right), with a classical gemological instrument. The analysis revealed a large vacuum core and highly irregular morphology, while further details were not easily recognizable. We then proceeded with the neutron tomography.

2.2. Neutron imaging setup

The MCP detector is capable to detect the transmitted neutron intensity behind the specimen as a function of neutron time-of-flight (TOF) or energy, since the flight path is a known parameter. The resulting pattern, normalized for the incident neutron intensity, maps the wavelength dependence of the material attenuation coefficient, which can be used to recover important information about the constituents of the sample.

Table 1
Gemological properties of the pearl.

Species and variety	Souffle-bead cultured pearl
Environmental	Freshwater
Shape	Baroque
Measurements	16.20 × 20.45 × 11.05 mm
Weight	22.58 ct
Drilling	None
Body color	Orange
Overtone	Rosee

The electronic readout of the Timepix, is constituted by a matrix of pixels, each of which has a 14 bit register able to store time of event arrival relative to the external trigger (timing of the neutron pulse in our experiments), when operating in "event timing" mode. The data acquisition time, or shutter period, can be arbitrarily set inside the time frame of a single neutron pulse generated by the source operating at 10 Hz frequency. At the end of each shutter period, data must be transferred from the Timepix to the data processing unit, based on a field-programmable gate array (FPGA). This process requires 320 μs to be completed and during this dead time, no further data can be acquired. Only one event per pixel per shutter is allowed for that generation of electronics. Therefore, these shutter periods must be carefully arranged in case of relatively high neutron flux to avoid event overlaps. That is the case for the IMAT instrument, where neutron flux is higher than 10^7 neutrons/cm^2/s. In the case of a high number of incoming neutron events, the events arriving later in the acquisition shutter period have lower probability to be detected as some pixels are already occupied by previous events. This phenomenon has been defined as "overlap effect" and described by Tremsin et al. in [14]. Such effect can be mitigated by decreasing the acquisition time, in other words the occupation probability per pixel per period. In this case, a greater number of shutter periods must be set in order to cover the whole pulse time frame, thus introducing remarkable gaps into the spectrum. A compromise must be taken between the number and the duration of the shutter periods.

Since the principal element of the sample was known to be aragonite, as shown in [7], the start and the end times of each shutter period were chosen in order to avoid the main Bragg edges of aragonite coinciding with the readout gaps. The information about the Bragg edges of aragonite was taken from the **ICSD** (the Inorganic Crystal Structure Database [15]), in which the crystallographic d-spacings of aragonite are reported. Taking into account the wavelength of the incoming radiation and the total flight path at IMAT, the most intense Bragg edges were expected to be generated by neutrons with TOF in between 55 ms and 80 ms. More details about the chosen shutter periods are shown in Table 2.

In [14], a procedure has been demonstrated to correct for the "overlap effect", with an important constraint. In fact, such a method can only be used when transmission data has been generated by neutron pulses with periodical and constant shape. Being this the case of IMAT beamline, the procedure has been successfully applied during post-processing operation via software to all the collected data sets.

2.3. Experimental setup

The sample was wrapped in an aluminum foil of 11 μm thickness to permit an easy manipulation of the specimen and allowing at the same time the radiography with neutrons, as aluminum is nearly transparent for neutrons (>99.9% transmission for such thin foil).

After that, the pearl was placed on a rotation stage (Fig. 2). The specimen to camera distance was 15 mm. With a beam collimation ratio L/D of 250 the geometric unsharpness was 60 μm with an effective neutron flux of about 5.9×10^6 n/cm^2/s. A set of 450 projections in the angular range 0°–180°, to fulfill the Nyquist-Shannon sampling theorem, were acquired within 315 s as exposition time. Moreover, a stack of six flat field images (three before and three after the tomography scan) with the same acquisition time were collected for normalization purposes.

Table 2
Shutter periods of the TIMEPIX. Start and end points are intended with respect to the external trigger of the neutron source. The IMAT beamline is located at ISIS Target Station 2 (TS2), where pulse repetition rate is 10 Hz.

Shutter period #	Start [ms]	End [ms]
1	10.00	24.68
2	25.00	47.68
3	48.00	95.00

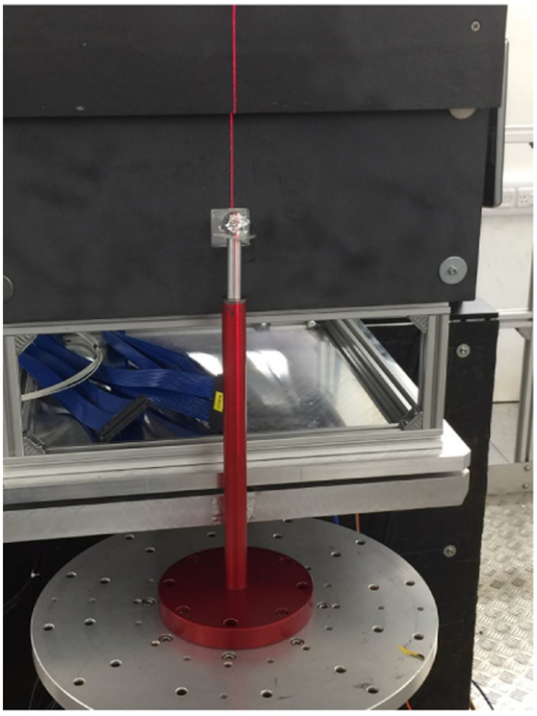

Fig. 2. Experiment setup. The pearl is placed on the rotating platform, in front of the MCP detector window.

With these settings, a total amount of about 36 h was required for the collection of an energy-dispersive tomography.

2.4. Tomographic reconstruction

The 450 projections have been corrected after the acquisition for the overlap effect.

We took into account the projections given by the complete spectrum of the transmitted neutrons in order to increase the statistics and obtain the neatest image reconstruction possible. To do this, we summed the projections with different energies for each angle-view. The flat-field correction was performed on the resulting dataset by simply dividing each projection by the average of the open beam images. Dead-pixels and gamma spots were removed from the normalized projections by using a median filter. The misalignment of the rotation axis with respect to the vertical detector axis and the defective pixels in the detector lead to reconstruction artifacts that appear in the reconstructed images as concentric rings and small circles, respectively. In order to avoid the artifacts, we applied to the dataset a ring removal filter based on combined wavelet and Fourier analysis [16], and determined the center of rotation. Both steps were performed in the MATLAB [17] framework. The tomographic reconstruction was finally performed by means of the Simultaneous Iterative Reconstruction Technique (SIRT) [18] implemented in the ASTRA TOOLBOX [19], an open source MATLAB and Python toolbox for 2D and 3D tomographic reconstruction.

3. Results and discussions

3.1. Virtual sections

In Fig. 3, we report a selection of six different virtual sections out of about 200 images obtained by the tomographic reconstruction. In these virtual sections the brightest regions represent the ones with higher neutron absorption and the darkest regions relate to voids or zones with lower neutron absorption. In our case, due to the biological nature of the sample, the brightest parts could be reliably associated

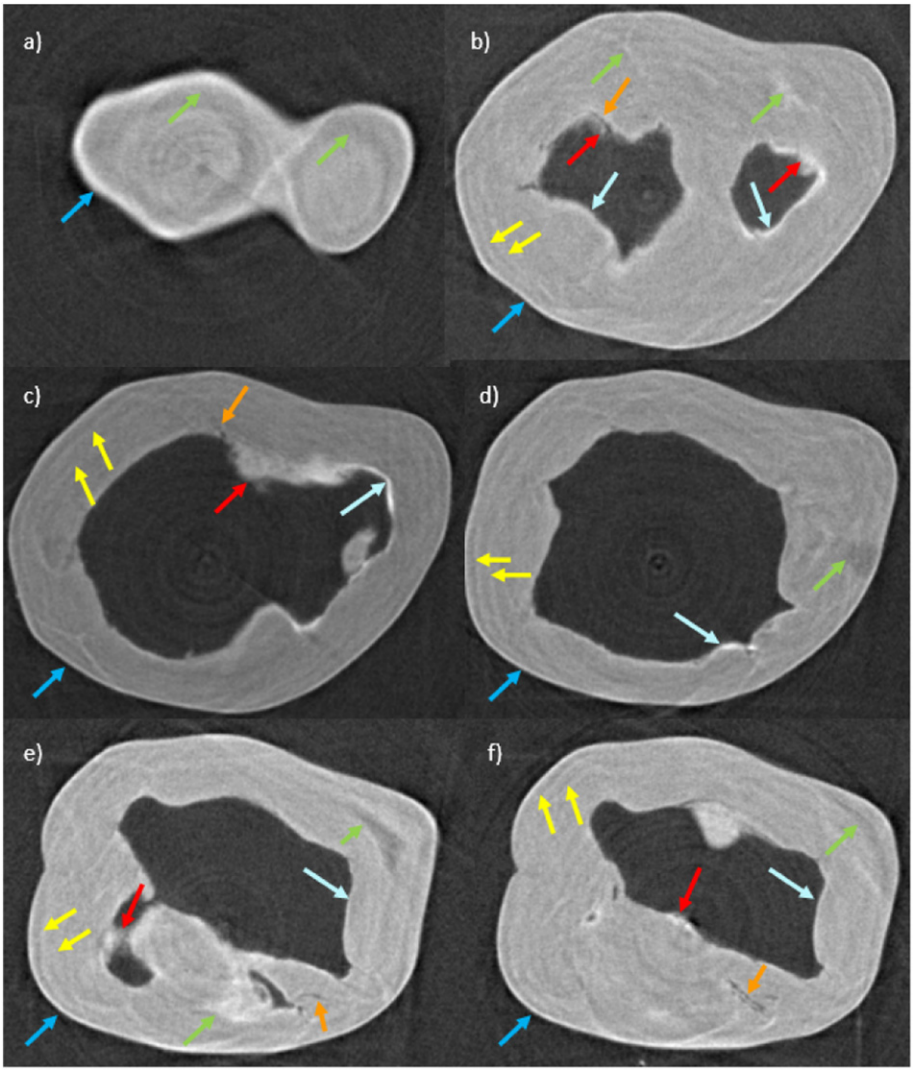

Fig. 3. a)–f) COLOR. Selection of six different virtual sections within the tomographic reconstruction. Many details of the pearl structures are evident. A full description is provided in the text.

with organic components of the pearl (maybe conchiolin fibres, a protein belonging to the group of keratins, tissue residues or other hydrogen containing compounds). As a general note, we noticed a recurrent artifact in our images, a pattern of concentric rings, that was supposed to be totally removed after the application of the ring removal filter during the tomographic reconstruction process. These structures were obviously not related to any real feature and have not been considered. The virtual sections, like any tomographic reconstruction, are taken at different positions or "height" of the sample. Our sequence from a) to f) follows a side of the pearl starting from the external part, towards the inner part.

In Fig. 3a) a section with a smaller area is visible, due to the external region investigated. Since our pearl has a very irregular morphology, in fact it has baroque shape, this virtual section reflects a sort of intersection of a bilobated structure. The area seems to be surrounded by a brighter part, probably an organic layer, which is visible in all the images a)–f) (marked by blue arrows). The area is not homogeneous, as evident in some parts highlighted by green arrows.

Fig. 3b) displays a virtual section towards the inner part of the pearl. Two voids are evident, again related to the bilobated nature of the sample. The voids contour is not regular nor clear. With light blue arrows we pointed out a sort of bright organic-rich rim, probably related to organic layers (either the ones from which the biogenetic mechanism of pearl production starts and/or the tissues deriving from the host mollusc). Moreover, some blurred parts (see red arrows) are organic-rich regions and may be related to remnants of a "soufflè" bead after degradation, or to the inhomogeneity in the first organic layer followed by aragonite platelets in a brick-like arrangement. Interestingly, we marked by yellow arrows some organic layers related to the pearl-formation process (concentric but not regular), mainly in the external part. The same is true also for the following virtual sections (again highlighted by yellow arrows). Finally, a fissure like structure is identified by an orange arrow.

Fig. 3c) exhibits a large central void, since we are approaching the central part of the pearl. Yet, a tomographic reconstruction provides a real size of the structure: we thus could derive a minimum nacre thickness of about 1.43 mm. Again, a red arrow indicates a very irregular contour zone, while an orange arrow identifies a fissure like structure.

Fig. 3d) has the most regular inner central void, with a rim (see light blue arrow). However, some irregular structures appear in the nacre (see green arrow) and organic-rich layers due to the pearl-formation process are still visible (see yellow lines).

Fig. 3e) displays a very inhomogeneous inner part: the central void is again displaying features of the very complex structure of this pearl, and of the bilobated nature (one central void, and other smaller voids too, or fissures – see orange arrow). Ring-like structures (yellow arrows), internal rim (light blue arrow), organic rich parts and bumps (red and green arrows) are evident.

Finally, Fig. 3f) exhibits again organic layering (see yellow arrows), an inner rim (light blue arrow), some bumps (see green arrow) and a fissure-like structure (see orange arrow). No rigid and regular bead was visible in any of the virtual sections, the core presenting mainly voids. Yet, we cannot exclude the presence of any compound in the inner regions, since it is reported that liquid/gaseous compounds can exit a soufflé pearl when drilled [12]. The neutron tomography has thus revealed a considerable amount of details of this baroque shaped pearl, very useful for the gemologists in the study of this kind of pearls. One third of the virtual slices obtained after the tomographic reconstruction was used to produce a movie, in order to clearly return the images of the whole pearl, section by section (see supplementary materials).

3.2. Energy-selective analysis

The characterization of the neutron transmission pattern versus the neutron wavelength has been performed on a separate set of radiographies collected for 4 h of radiation exposure on the specimen, in order to obtain good neutron statistics. Further, 4 h have been spent for the flat field radiography, for normalization purposes, which removes the features related to the beam spectrum and detector non-uniformities.

In Fig. 4 the Region Of Interest (ROI) related to both the center of the pearl and its external part is shown. When the central part is considered, the neutron beam is mostly perpendicular to the pearl organic layers.

The transmission pattern of the pearl core shows that the Bragg edges of aragonite, the most predominant phase of the nacre (over 95% by volume as told in (7)), related to the (201) plane (wavelength $\lambda = 5.40$ Å) is clearly visible, together with the one related to the (210) ($\lambda = 4.96$ Å).

By contrast, when the external ROI is considered, an increment of the intensity of a Bragg edge at different wavelengths is noticeable. A clear example is the increase of the mean transmittance at $\lambda = 3.95$ Å (122) and $\lambda = 2.34$ Å (0 2 6) with respect to the previous curve.

In the outer shell, the strong Bragg edge is smeared out. Instead of well-defined Bragg edges there is a broad hump in the transmission spectrum between 4.50 Å and 6.50 Å. This may be explained by the fact that scattering is redistributed, which indicates the presence of a preferred isoorientation of the crystallites. This is determined by the nacre platelets, confirming the aragonitic "brick-wall" structure of the nacres textures, as presented by Chateigner et al. [8].

The interpretation is related only to the ROI selected in the lower part of Fig. 4. On the other hand, the transmission patterns shown in the upper part of the same figure are detected in each pixel of the neutron counting detector. This enables the evaluation of the main Bragg edge intensity at 5.40 Å across the entire specimen with a spatial resolution of about the pixel size, i.e. 55 μm. Furthermore, such BE intensity is proportional to the aragonite phase amount across the sample.

A dedicated C++ program was developed in the data analysis framework ROOT [20], to take account of the spectral analysis of a large number of 512 × 512 pixels. Such framework is designed for storing and analyzing petabytes of data in an efficient way and

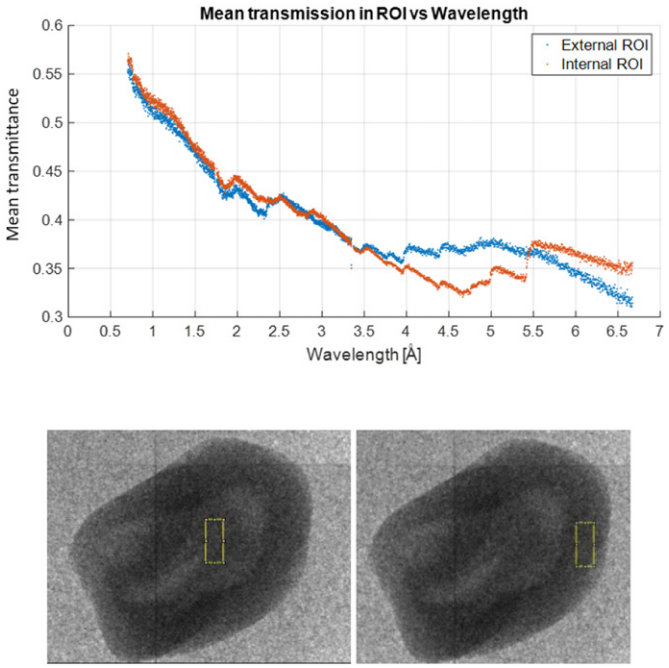

Fig. 4. COLOR. TOP: Neutron transmission spectra containing Bragg edges for both internal and external ROI of the pearl. BOTTOM: Internal and external ROI, corresponding to the core and the shell of the pearl.

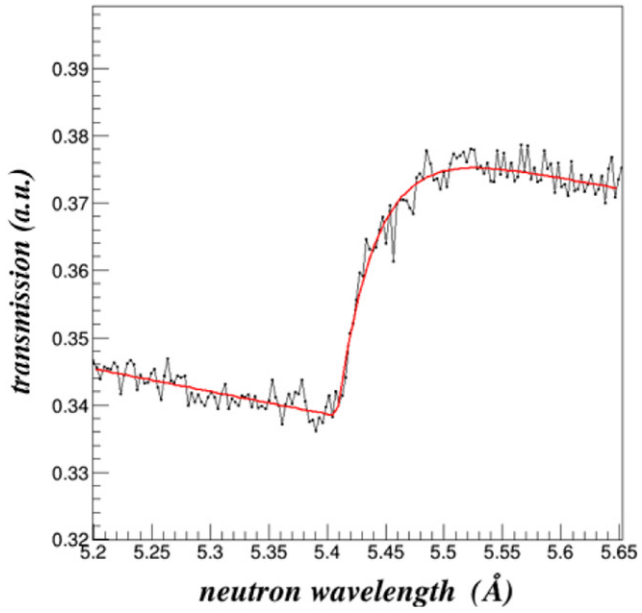

Fig. 5. Example of a Bragg edge fit for the main aragonite Bragg edge at 5.40 Å.

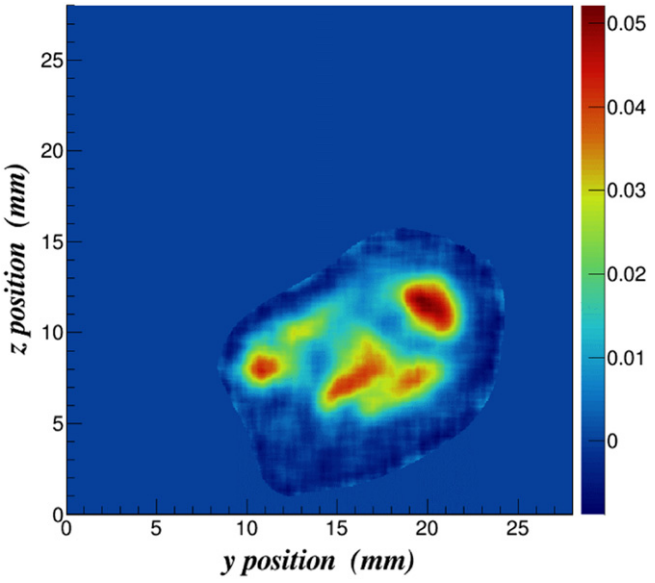

Fig. 6. COLOR. 2D map for the main aragonite Bragg edge intensities at 5.40 Å. Such map is proportional to the aragonite phase amount across the specimen.

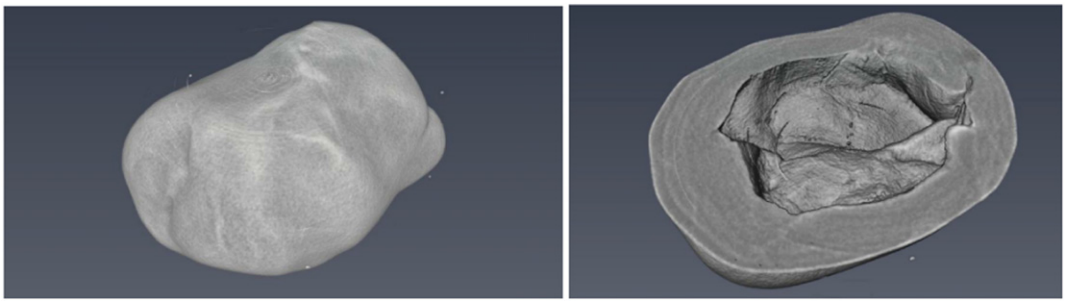

Fig. 7. Volume rendering of the pearl. Left: global view. Right: cut view. Here the empty core is clearly visible.

therefore suitable for such type of data analysis. For each pixel, a Bragg edge was fitted using the three-step procedure reported in [21]. An example of the fitting quality for a pixel within the specimen is reported in Fig. 5.

The intensity of the Bragg edge was extracted by the difference in the transmission values after and before the edge. The recursive application of the same fitting procedure, for all pixels, enables the generation of a 2D map of the Bragg edge amplitude reported in Fig. 6 and therefore provides further information about the aragonite phase distribution within the specimen [22]. In this figure, we followed for x and y axis the conventional direction used for the sample positioner system (SPS) available on the IMAT instrument. In fact, the beam direction, according to this convention, is along the x-axis. The color scale of the figure reflects the amplitude of the analyzed Bragg edge, showing that the family of planes related to the Bragg Edge at 5.40 Å of the aragonite phase is more concentrated in the central ROI, while it is less present in the outer ROI. This confirms the observations obtained with the 1D data analysis of Fig. 4.

3.3. 3D volume reconstruction

For visualization and analysis purposes, the reconstructed slices were loaded into the Amira-Avizo 3D software [23]. The volume rendering of the pearl is shown in Fig. 7. The vertical cut shown in the right panel of the same figure clearly shows that the core is either empty or filled with a material different to the one constituting the pearl nacre. This volume rendering confirms the "soufflé" structure of the pearl.

4. Conclusions

In this work, we explored the inner morphology of a baroque-shaped soufflé pearl. This very complex sample was very suitable to demonstrate the potential of energy-selective neutron imaging on biological samples. The tomographic reconstruction of a pearl showed numerous features of the pearl inside its bulk and allowed the 3D volume rendering, exhibiting an empty core, characteristic of the "soufflé" pearls. Many other details could be used by gemologists to infer the pearl-growing process for this pearl, in a completely non-destructive way. Moreover, the phase mapping of aragonite permitted the visualization of its crystallographic orientation inside the specimen and the study of its microstructural properties. Yet, only an energy-selective technique could discriminate between the presence of different phases and localize them in the inner part of this kind of specimen. Further studies, including phase mapping related to other phases (such as calcite) constituting the pearl and the reconstruction at different energies will be conducted in the future to obtain a more complete and global description of such a biological specimen.

Supplementary data to this article can be found online at https://doi.org/10.1016/j.microc.2017.12.002.

Acknowledgments

The CNR-STFC agreement 2014–2020 (No. 3420 2014–2020) concerning collaboration in scientific research at the ISIS Spallation Neutron Source is gratefully acknowledged.

References

[1] Materials analysis opportunities on the new neutron imaging facility IMAT@ISIS, T. Minniti, W. Kockelmann, G. Burca, J.F. Kelleher, S. Kabra, S.Y. Zhang, D.E. Pooley, E.M. Schooneveld, Q. Mutamba, J. Sykora, N.J. Rhodes, F.M. Pouzols, J.B. Nightingale, F. Aliotta, L.M. Bonaccorsi, R. Ponterio, G. Salvato, S. Trusso, C. Vasi, A.S. Tremsin, G. Gorini, J. Instrum. 11 (March 2016)https://doi.org/10.1088/1748-0221/11/03/C03014.
[2] A.S. Tremsin, J.B. McPhate, J.V. Vallerga, O.H.W. Siegmund, J.S. Hull, W.B. Feller, E. Lehmann, Detection efficiency, spatial and timing resolution of thermal and cold neutron counting MCP detectors, Nucl. Instrum. Methods Phys. Res., Sect. A 604 (2009) 140–143, https://doi.org/10.1016/j.nima.2009.01.041.
[3] X. Llopart, R. Ballabriga, M. Campbell, L. Tlustos, W. Wong, Timepix, a 65k programmable pixel readout chip for arrival time, energy and/or photon counting measurements, Nuclear Instruments and Methods in Physics Research, Section A: Accelerators, Spectrometers, Detectors and Associated Equipment 581 (1–2 SPEC. ISS.) (2007) 485–494, https://doi.org/10.1016/j.nima.2007.08.079.
[4] A.S. Tremsin, J.V. Vallerga, J.B. McPhate, O.H.W. Siegmund, R. Raffanti, High resolution photon counting with MCP-timepix quad parallel readout operating at >1 KHz frame rates, IEEE Trans. Nucl. Sci. 60 (April 2013)https://doi.org/10.1109/TNS.2012.2223714.
[5] A.S. Tremsin, J.B. McPhate, J.V. Vallerga, O.H.W. Siegmund, W.B. Feller, H.Z. Bilheux, J.J. Molaison, C.A. Tulk, L. Crow, R.G. Cooper, D. Penumadu, Transmission Bragg edge spectroscopy measurements at ORNL spallation neutron source, J. Phys. Conf. Ser. 251 (2010)https://doi.org/10.1088/1742-6596/251/1/012069.
[6] J.R. Santisteban, L. Edwards, V. Stelmukh, Characterization of textured materials by TOF transmission, Phys. B Condens. Matter 385–386 (2006) 636–638, https://doi.org/10.1016/j.physb.2006.06.090.
[7] H. Kakisawa, T. Sumitomo, IOP Publishing, The toughening mechanism of nacre and structural materials inspired by nacre, Sci. Technol. Adv. Mater. 12 (January 26, 2011)https://doi.org/10.1088/1468-6996/12/6/064710.
[8] D. Chateigner, C. Hedegaard, H.R. Wenk, Mollusc shell microstructures and crystallographic textures, J. Struct. Geol. 22 (2000) 1723–1735.
[9] E. Strack, Pearls, Ruhle-diebener-Verlag, 2006 87.
[10] N. Sturman, The microradiographic structures of non-bead cultured pearlsa, Lab Notes, August 20, 2009.
[11] K. Scarratt, T.M. Moses, S. Akamatsu, Characteristics of nuclei in Chinese freshwater cultured pearls, Gems & Gemology 36 (2) (2000) 98–109.
[12] N. Sturman, E. Strack, "Soufflé" freshwater cultured pearls, Gems & Gemology 46 (2) (2010) 61–63.
[13] L.E. Cartier, M.S. Krzemnicki, New developments in cultured pearl production: use of organic and baroque shell nuclei, Aust. Gemmol. 25 (1) (2013).
[14] A.S. Tremsin, J.V. Vallerga, J.B. McPhate, O.H.W. Siegmund, Optimization of Timepix count rate capabilities for the applications with a periodic input signal, J. Instrum. (May 2014) 9.
[15] FIZ Karlsruhe, ICSD – the inorganic crystal structure database, https://www.fiz-karlsruhe.de/de/leistungen/kristallographie/icsd.html [Online].
[16] B. Münch, P. Trtik, F. Marone, M. Stampanoni, Stripe and ring artifact removal with combined wavelet-Fourier filtering, Opt. Express 17 (2009) 8567, https://doi.org/10.1364/OE.17.008567.
[17] MathWorks, *https://www.mathworks.com/products/matlab.html* [Online].
[18] P. Gilbert, Iterative methods for the three-dimensional reconstruction of an object from projections, J. Theor. Biol. 36 (1972) 105–117, https://doi.org/10.1016/0022-5193(72)90180-4.
[19] W. van Aarle, W.J. Palenstijn, J. Cant, E. Janssens, F. Bleichrodt, A. Dabravolski, J. De Beenhouwer, K.J. Batenburg, J. Sijbers, Fast and flexible X-ray tomography using the ASTRA toolbox, Opt. Express 24 (22) (2016) 25129–25147.

[20] ROOT, I. Antcheva, M. Ballintijn, B. Bellenot, M. Biskup, R. Brun, N. Buncic, Ph. Canal, D. Casadei, O. Couet, V. Fine, L. Franco, G. Ganis, A. Gheata, D.G. Maline, M. Goto, J. Iwaszkiewicz, A. Kreshuk, D. Marcos Segura, R. Maunder, L. Moneta, A. Nauman, E. Offerman, V. Onuchin, S. Panacek, F. Rademakers, P. Russo, M. Tadel, A C++ framework for petabyte data storage, statistical analysis and visualization, Comput. Phys. Commun. 180 (2009) 2499–2512.
[21] J.R. Santisteban, L. Edwards, A. Steuwer, P.J. Withers, Time-of-flight neutron transmission diffraction, J. Appl. Crystallogr. 34 (2001) 289–297.
[22] R. Woracek, D. Penumadu, N. Kardjilov, A. Hilger, M. Boin, J. Banhart, I. Manke, 3D mapping of crystallographic phase distribution using energy-selective neutron tomography, Adv. Mater. 26 (2014) 4069–4073, https://doi.org/10.1002/adma.201400192.
[23] FEI, https://www.fei.com/software/amira-avizo/ [Online].